International Journal of Thermal Sciences 205 (2024) 109289

Contents lists available at ScienceDirect

International Journal of Thermal Sciences

journal homepage: www.elsevier.com/locate/ijts

Analysis of the ice front propagation in heart tissues: First results

F. Barbero [a], G. Verona Rinati [a], G. Bovesecchi [b,*], S. Corasaniti [a], M. Potenza [a], P. Coppa [a], C. Pisano [c]

[a] Department of Industrial Engineering, University of Rome "Tor Vergata", Via Del Politecnico 1, 00133, Rome, Italy
[b] Department of Enterprise Engineering, University of Rome "Tor Vergata", Via Del Politecnico 1, 00133, Rome, Italy
[c] Department of Surgical Sciences, University of Rome "Tor Vergata", Via Montpellier 1, 00133, Rome, Italy

ARTICLE INFO

Keywords:
Cryo-ablation
Cryoballoon
Heat transfer
Ice front
Finite differences
Atrial fibrillation

ABSTRACT

Experimental tests were conducted simultaneously using an infrared (IR) camera and a standard camera in the visible range (VR) to detect the ice front propagation as a function of time and space in different sections of pig heart laid on the surface of a cold spherical aluminum source (30 mm in diameter). The goal of the experiments was to simulate the conditions during the medical practice of internal cryotherapy, which aims to eliminate the tissues responsible for atrial fibrillation in the human heart. Freezing temperatures and related times were also measured, although they were affected by several uncertainties associated with the tests, such as air trapping between the metal sphere and flesh, inhomogeneity of the flesh samples, and the low spatial resolution and accuracy of the IR camera. A comparison with the results of previously conducted numerical simulations (Potenza et al., 2023) [1] is also discussed.

1. Introduction

Cryoablation has become a recurrent method for treating atrial fibrillation in human hearts [1]. This surgical procedure can be performed either by catheter insertion in a pulmonary vein (internal cryotherapy) or during open-heart surgery (external cryotherapy). Internal cryotherapy is conducted using a cryo-balloon, with a maximum diameter of 30 mm, inserted in the left atrium, and insufflating nitrous oxide for 60–80 s, producing temperatures as low as −50 °C due to the Joule-Thomson isenthalpic expansion [2]. Two systems are currently in use: the Artic Front™ (Medtronic, USA) [3] and the Polarix™ (Boston Scientific, USA) [4]. A comparison between the two is reported in Ref. [5].

The procedure aims to eliminate the nerve cells responsible for the patient's arrhythmia by freezing them. However, this can lead to dangerous drawbacks, such as the reduction (or "stenosis") of the pulmonary vein size [6] and lesions to the nearby phrenic nerve [7–9]. To reduce these risks, accurate control of the ice front progression over time is crucial.

A simple numerical model simulating the freezing of cardiac tissues [10], which also considers metabolic activity and blood perfusion in the unfrozen areas, has been developed using Pennes's bio-heat equation [11] and solving it through a finite difference procedure in a cubic grid. This model simulates the phase transition with effective heat capacity [12], using an approach similar to that of Deng and Liu [13]. The results showed that the propagation speed of the ice front is highly dependent on the freezing temperature and heat removal, with negligible contributions from metabolic activity and blood perfusion.

Freezing temperatures of flesh reported in the literature still exhibit significant uncertainties. According to various authors [14–17], the freezing of human biological tissues occurs within a broad temperature range (from −1 to −8 °C) due to the inhomogeneity of the structure. Intracellular and extracellular fluids and molecules have different freezing points, leading to an inhomogeneous freezing process at the ice front.

The causes of cellular death by freezing remain a subject of debate [18] and depend on various factors such as the surrounding temperature, duration, and specific organs involved. The most cited cause of cellular death is the perforation of the cell membrane by sharp ice micro-crystals forming inside and outside the cells during the freezing transition.

Thus, measuring or predicting the ice front position over time is crucial, as it helps localize where and when the cells, including the nerves responsible for fibrillation, are killed, while minimizing damage to surrounding areas.

The literature provides a range of freezing temperatures from −8 °C

* Corresponding author.
E-mail address: gianluigi.bovesecchi@uniroma2.it (G. Bovesecchi).

https://doi.org/10.1016/j.ijthermalsci.2024.109289
Received 11 April 2024; Received in revised form 29 June 2024; Accepted 17 July 2024
Available online 19 July 2024

to −1 °C. Altman & Dittmer [16] and Wessling & Blacksehar [17] report an upper limit between −0.5 °C and −1 °C and a lower limit between −5 °C and −8 °C. This wide range significantly impacts the numerical modeling of ice front propagation.

The goal of this paper is to detect and process the temperature profiles over time of a raw, freshly slaughtered piece of pig cardiac tissue during freezing to track the time-varying position of the ice front.

Previous numerical simulations [10] judged the effects of metabolic activity and blood perfusion negligible, at least in limited spaces and times. In the described experiments, only a few cubic millimetres of tissue are involved, and the duration is on the order of tens of seconds. Therefore, both metabolic heat and blood perfusion can be safely neglected in real experiments, allowing the use of dead tissues.

The rationale behind the authors' work in this field includes.

1. Numerical modelling of the cryo-ablation process under clinical conditions, as reported in Ref. [10].
2. Experimental testing of a similar procedure. Unfortunately, the experimental conditions of the tests (cold finger temperature and heat removal speed) do not strictly correspond to the clinical ones.
3. The tested experimental conditions will be simulated with a new numerical model, and a comparison with the experimental results will be conducted. This corresponds to numerical model calibration, evaluating specific process parameters (heat power removed, times, and temperatures), enabling accurate simulation of true clinical conditions. This will be the subject of further work.

2. The experiments

Pig hearts are quite similar to human hearts, both in size and shape [19]. Thus, from a cellular point of view, the differences in heat transfer are assumed to be negligible. Experiments were carried out on unfrozen samples of hearts from daily slaughtered pigs obtained from a local slaughterhouse, accompanied by a "non-food purposes" self-declaration to avoid strict EU regulations regarding food and meat. The pig hearts used for experiments were from 12-month-old animals of the "Large White" breed, which is standard for slaughtered pigs in Italy. The thermophysical properties of both human and pig tissues are nearly the same, regardless of age, breed, or tissue location. More significant differences are found depending on the type of tissue examined, such as connective, bone, or muscle.

The sketch of the experimental apparatus, including the various instruments, is shown in Fig. 1.

An aluminum cold finger (CF), 30 mm in diameter at the spherical end (matching the maximum extension of the cryo-balloon), was manufactured (Fig. 2a) and connected to a freezing system (Fig. 2b). Two thermocouples (Fig. 1c) were placed on the cold finger to monitor its surface temperature. At ambient humidity and temperatures of −50 °C or lower, the CF quickly becomes surrounded by ice crystals (Fig. 2d) due to the freezing of air moisture. To avoid the unpredictable insulating effect of this ice layer, practical methods were employed, such as covering the finger with aluminum foil (Fig. 2e) and removing it just before the tests, or manually removing the ice. This ensured better direct contact between the CF and the flesh, although the reproducibility of this method was limited.

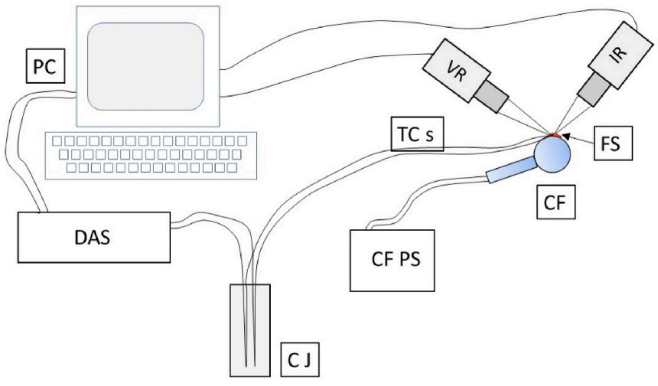

Fig. 1. Sketch of the experimental setup: PC (personal computer); DAS (data acquisition system); CF PS (cold finger power supply); dewar with CJ (thermocouple cold junction); TCs (thermocouples); CF (cold finger); VR (visible range camera); IR (infrared camera); FS (tested flesh strip).

The full experimental setup includes a visible range camera (VR camera) to track the ice front (Fig. 2f), an infrared camera (IR camera, Fig. 2g) to record temperature maps, and two thermocouples (TCs) to measure temperatures at the CF-flesh interface and in the air, respectively. Other authors [20] have used another optical method, Digital Holographic Interferometry (DHI), to observe the shape and progress of the ice ball created during cryosurgery for tumor ablation. However, as described in section 2.2.1, the ice front propagation is also easily identifiable from the visible camera images, as shown in Fig. 3.

Strictly speaking, the IR camera records radiance temperature, and the true temperature is obtained by accounting for the source emissivity. Generally, all tissues, both living and dead, exhibit high emissivity values in the range of 0.95–0.99, primarily due to their high-water content [21]. This is similar to most foods. Therefore, no correction for emissivity was necessary.

Since the main goal of the research was to detect and record temperatures at the phase-change interface, preliminary tests were conducted by inserting thermocouples with hot junctions of 0.3 mm in diameter into the flesh. The initial idea was to recognize a plateau indicating the phase-change in the temperature vs. time graphs. Unfortunately, this approach was unsatisfactory due to the large size of the thermocouple hot junction and the brief transient period caused by the high thermal power removed by the CF heat sink.

After ruling out the possibility of recognizing the freezing temperature from the thermocouple recordings, it was decided to record the freezing of the heart pieces in the visible range with the VR camera (Fig. 2f). However, flesh is not transparent, and thermocouples were visible only when extremely close to the surface, leading to border effects. Additionally, before freezing and at such small scales (fractions of millimetres), the flesh was extremely soft, gelatinous, and fragile. It was very difficult to maintain the same position of the thermocouple for the few seconds required for these measurements. Even the simple weight and elastic tension of the TC cables caused the thermocouple tip to move fractions of a millimetre inside the sample.

Ultimately, thermocouples were still used, but only to measure the flesh/CF interface and the outer boundary condition with air.

2.1. Devices and software

Most of the VR camera recordings are in QuickTime File Format (QTFF) with a ".mov" extension, at a resolution of 1920x1080 pixels and a frame rate of 30 frames per second (more precisely, 29.98 frames/s). The resolution and quality of VR camera images are much better than those of the IR camera. Consequently, even when replacing the VR professional reflex camera (Fig. 2f) with an iPhone 6, the video quality was excellent and did not affect the collected data. One pixel of the VR camera corresponds to a square with a 0.046 mm side, while one pixel of the IR camera corresponds to a square with a 0.141 mm side. Thus, the bottleneck was due to the IR camera rather than the VR camera.

The IR camera (Fig. 1g) was a FLIR A6751 (P/N: 29440-251) [22], with a temperature range from −20 °C to +350 °C and a factory-declared accuracy of ±1 °C for temperatures below 100 °C. Generally, all FLIR cameras are described as having a typical accuracy no better than ±1 °C. Calibration of the device with black bodies was not performed, although it could have reduced the error or better quantified it.

The software "FLIR ResearchIR Max" [23], supplied with the IR

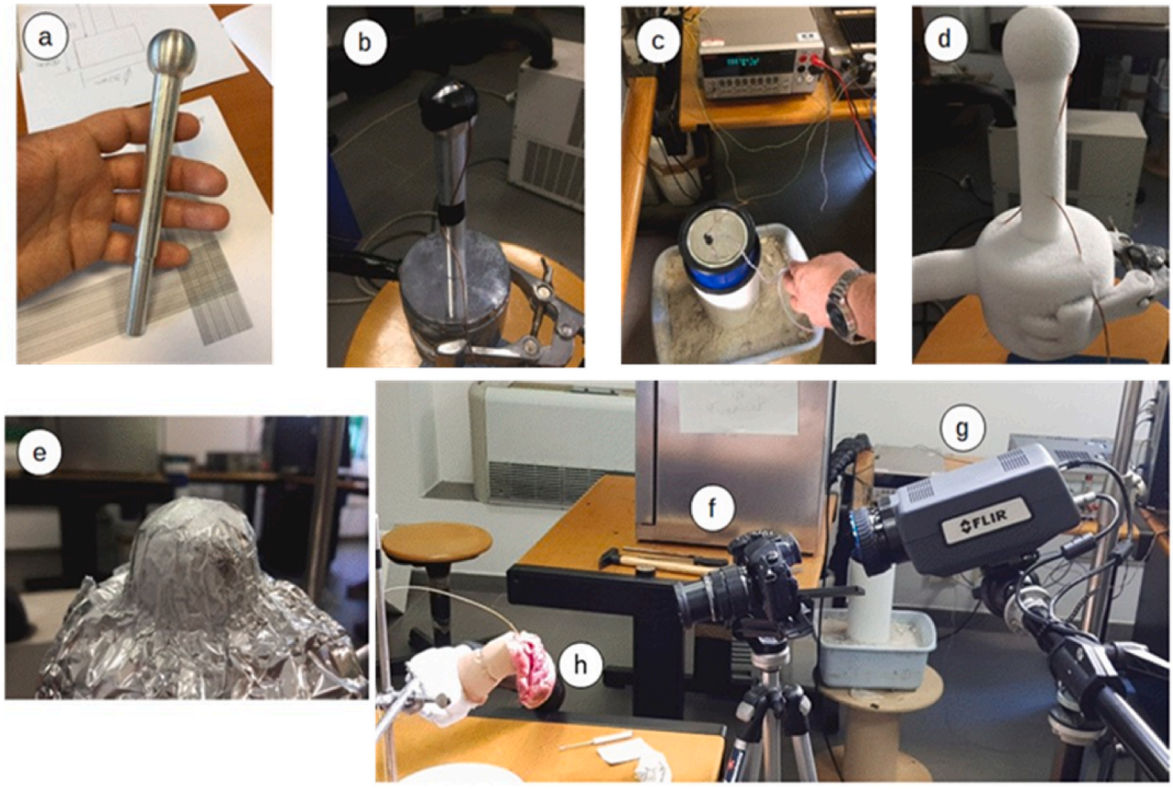

Fig. 2. Devices (a, b, c, d, f, g) and pig heart (h) used for the experiments.

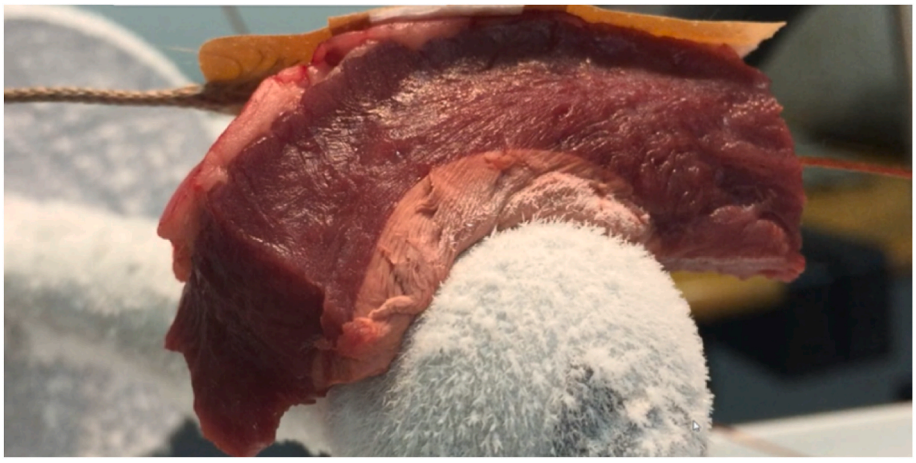

Fig. 3. Photo of a cardiac muscle piece placed on the cold finger after 20 s, clearly showing the ice front.

camera, was used to record the IR images. Each IR image, corresponding to one time frame, was processed using self-developed computer programs in the Scilab [24] and Mathematica [25] environments. The VR camera images were also processed with the same computer programs.

2.2. Tests

Two series of tests were conducted on pig heart tissues: one series on the left atrial section (4.5 mm thick) and the other on the ventricular section (30 mm thick). The two types of samples exhibited different cellular structures: primarily connective tissue in the former, where cryoablation is performed, and muscle tissue in the latter.

Data processing involved evaluating temperatures in different sections from the IR images at various time points. By interpolating these images at times t and radial distances d from the CF, a continuous 3D surface is obtained, described by equation (1):

$$T = T(d, t) \tag{1}$$

Simultaneously, using VR images, the distance of the ice front d_f from the CF is interpolated using a continuous and strictly monotonic function.

$$d_f = d_f(t) \tag{2}$$

as well as times are interpolated by the inverse of the previous function.

$$t_f = {d_f}^{-1}(d) \tag{3}$$

As a consequence, the ice front temperature can be expressed both as a function of time t

$$T_f = T\left(d_f(t), t\right) \equiv T_f(t) \tag{4}$$

and as a function of the distance d from the CF.

$$T_f = T\left(d, d_f^{-1}(d)\right) \equiv T_f(d) \tag{5}$$

Eqs. (1) and (2) were used to process data of atrial connective tissue, while all equations from (1) to (5) of the mussel ventricular tissue.

2.2.1. Left atrium connective tissue

Two different samples were extracted from the tissue of the pig hearts where the pulmonary vein inserts into the atrium (the location of cryoablation). The VR and IR images of the samples are shown in Fig. 3, along with the VR strips used to identify the ice front.

The average thickness of the left atrium wall, approximately 4–5 mm, and the IR video resolution of 0.141 mm meant that the IR image of the tissue across its thickness was represented by only 28 pixels. While sufficient for measuring the propagating ice front, this resolution was inadequate for reliably measuring the ice front temperature, especially where the temperature gradient was steep.

The sample sections (whose temperatures are depicted in Fig. 5) are marked as green lines in Fig. 4 and correspond to the section where the ice propagated most rapidly. This section was expected to have the best contact between the CF and flesh. The ice front propagation shown in Fig. 5d was derived from inspecting the VR video and capturing frame strips at different times, as shown in Fig. 4c.

Temperatures recorded by the TCs are shown in Fig. 5a. In the first test, the CF temperature ranged from −87.5 °C (0 s) to −84 °C (30 s), and in the second test, from −81 °C (0 s) to −76 °C (30 s). Variability in the refrigeration system's performance contributed to the difficulty in achieving consistent starting temperatures. Despite these differences, both curves exhibit a similar trend in temperature increase time (from 18 to 24 s) and asymptotic ΔT reached (between 3.5 and 5 °C). Variations between the temperatures and trends could be attributed to differences in the thickness of the air layer trapped between the CF and flesh, influenced by the presence of ice crystals.

Fig. 5b and c show the trends of equation (1) at different times t, while Fig. 5d displays the trends of the ice front from equation (2). It is notable that during the initial cooling, the first layer, which is 0.5–1 mm thick, exhibits a non-uniform temperature profile. In Fig. 5d, the trends of the ice front after the first 10 s show consistent slopes, despite initial transient differences, likely influenced by the contact between the flesh and the CF and the presence of trapped air.

It is important to emphasize that during actual cryosurgery operations, no air is present in the effective working environment.

2.2.2. Ventricular muscle tissue sections

Since the cardiac muscle tissue is much thicker than the vein wall and considering the substantial weight of the slaughtered pig (approximately 150 kg), it was feasible to extract 30 mm thick samples, as depicted in Fig. 3. Two samples underwent examination using a procedure analogous to that depicted in Fig. 5 for the connective tissue. The results of these two tests are presented in Fig. 6, along with the assessed dispersion (refer to the uncertainty analysis in Chapter 3). The primary curves are depicted centrally in orange, showcasing a typical progression: initially, highly variable temperatures (ranging from 0 to −10 °C), followed by relatively stable values (between −4 and −6 °C) after the first minute. Ultimately, the central curve in Fig. 6 illustrates various trends, highlighting the ice front temperature over time.

To assess uncertainties stemming from IR and VR collimation and synchronization, upper and lower curves with ± Δx are included alongside the primary curve, as depicted in Fig. 6a and b. Similarly, Fig. 6c and d show trends for ± Δd.

The fairly constant temperature observed after the first minute (between −4 °C and −6 °C) can be considered as the freezing temperature. This range aligns with the previously mentioned uncertainty in detecting the ice front temperature [14–17].

Fig. 7a and b exhibit trends similar to those in Fig. 5b and c. In these figures, the black line represents the freezing temperature T_f versus distance from the CF, as detected from VR camera images. The differently colored curves correspond to different time points, each 1 s apart. Fig. 7c and d depict overlapped trends of the ice front evolution, similar to Fig. 5d for the connective tissue.

Both Figs. 6 and 7 demonstrate that initial temperature values near the CF (within 1 mm and during the first 10 s) exhibit significantly higher uncertainty, ranging from −5 °C to −20 °C, due to the challenges in detecting these temperatures owing to their variability. A more detailed assessment of this uncertainty, along with other sources of uncertainty, is provided in Section 3.

3. Uncertainty analysis and comments of results

The primary challenge in data processing was synchronizing the acquisition between the visible (VR) and infrared (IR) cameras, given their differing viewpoints and spatial resolutions (0.141 mm for IR and 0.046 mm for VR, as discussed in Section 2.1). To ensure consistency in time resolution, both cameras were interpolated to a 0.1-s time step to prevent discrepancies in image acquisition. Through numerous iterative attempts, the following uncertainties were identified: radial distance resolution $\Delta d = 0.141$ mm, tangential $\Delta x = 0.423$ mm (three times the spatial resolution), and time $\Delta t = 0.1$ s. Synchronization between IR and

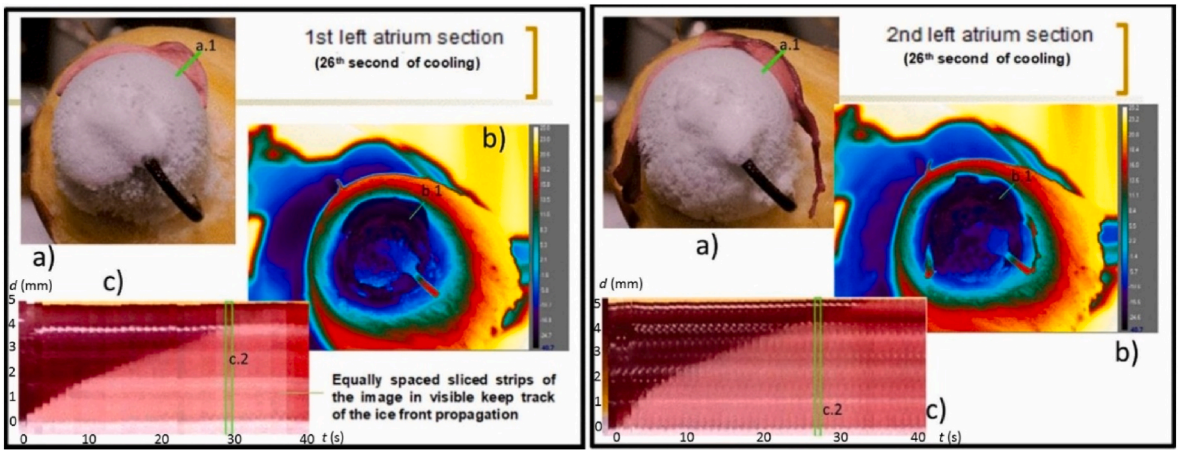

Fig. 4. Two repetitions of the tests on atrial connective tissue. a): VR images; b), IR images. Green lines a1 and b1shows the flesh sections where data were collected, and reported in Fig. 4 c. The vertical strips c), taken from VR different frames, were used to identify the ice front. One example of this detection is the green marked strip c2). The strips reproduced in the c) images are obtained by the a) photos.

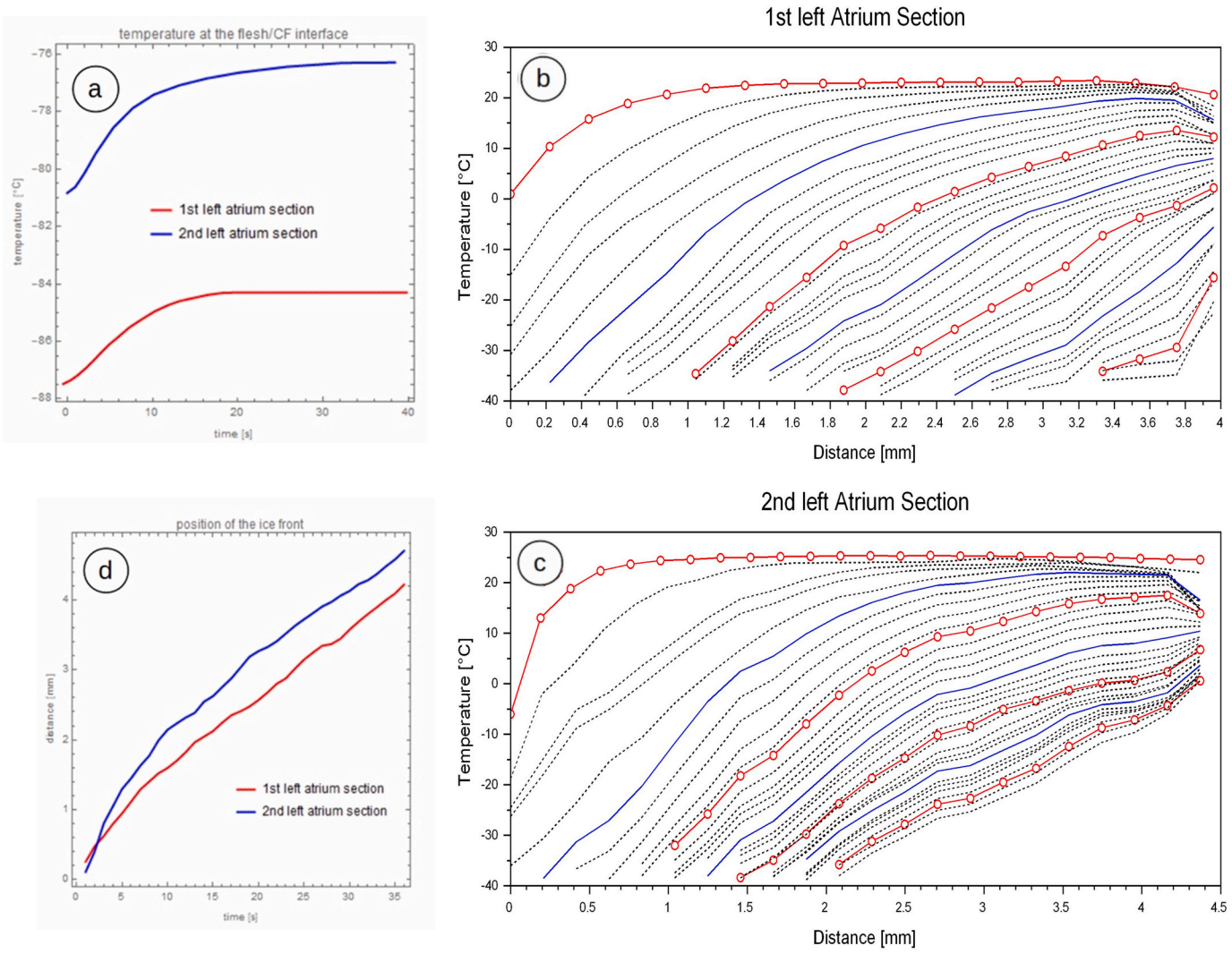

Fig. 5. (a) Data of thermocouples located on the CF surface; (b) and (c): IR readings of two different sections of the left atrium: red lines every 10 s, blue lines every 5 s and black dotted ones every 1 s; (d): ice front detected with the VR camera.

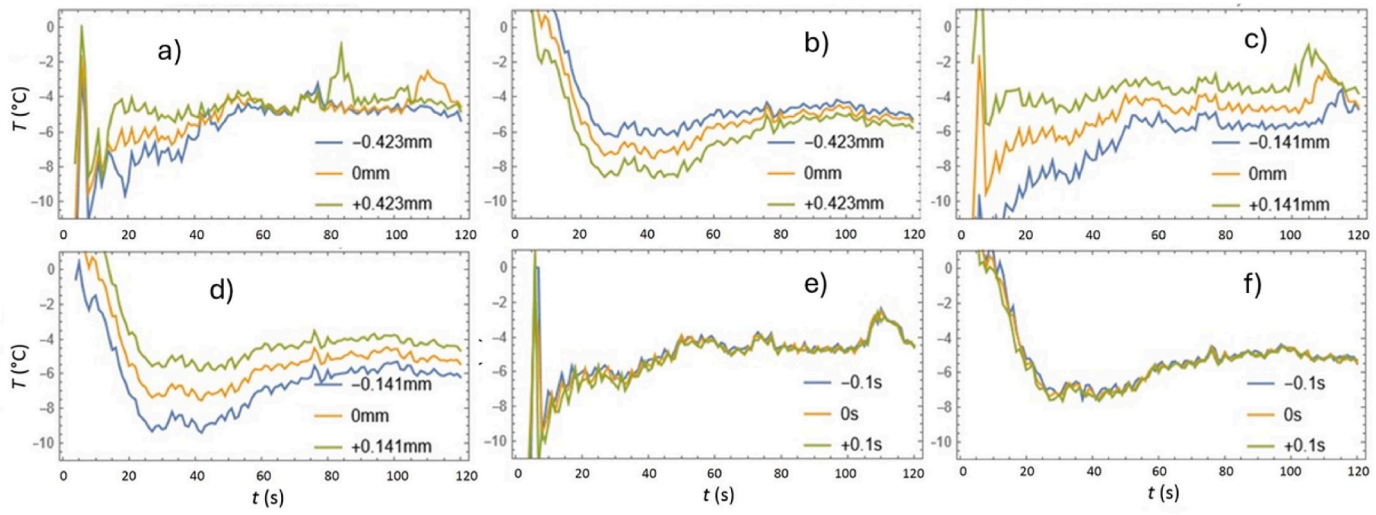

Fig. 6. (a, c, e) first sample; (b, d, f) second sample; (a, b) ice front temperature as a function of time, with added an upper and lower curve at ± Δx; (c, d) same trends with ± Δd; (e, f) uncertainty due to time synchronization between visible and IR.

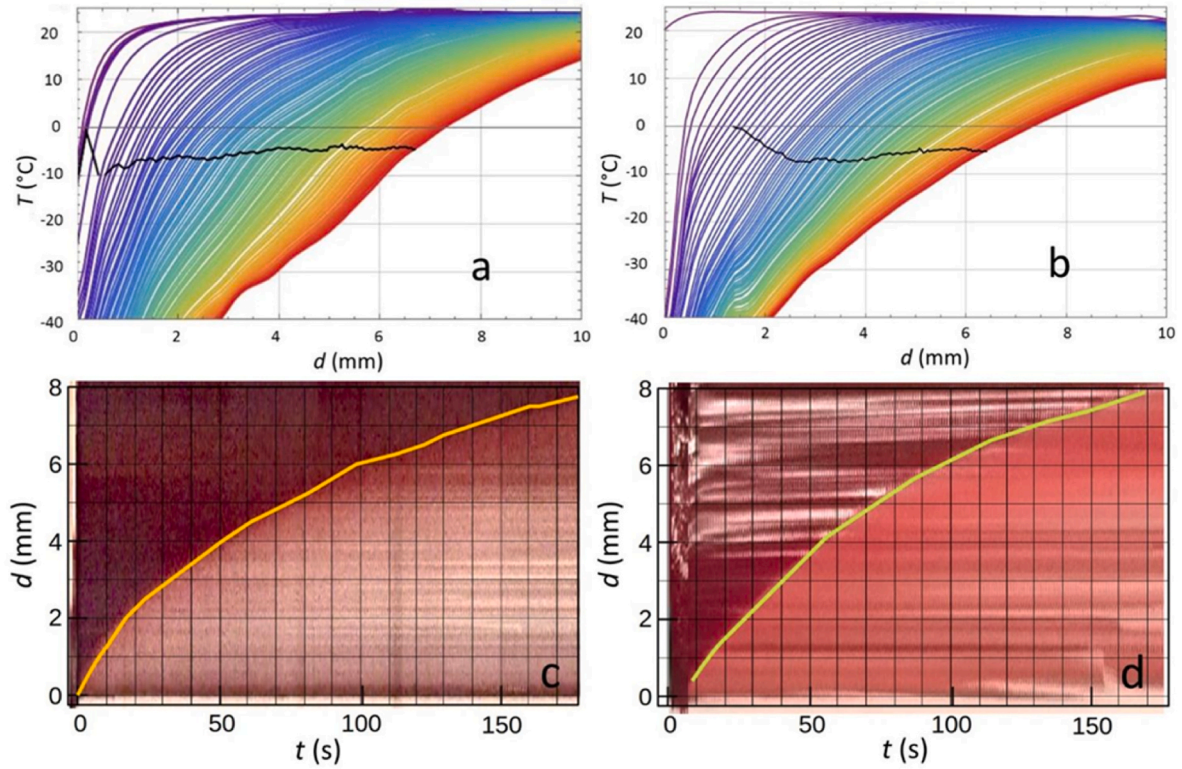

Fig. 7. Muscle tissue flaps: Average IR profiles of temperatures (T) as a function of radial distance (d) from the cold finger, colored from blue (0 s) to red (160 s) every 1 s, and the ice front, in black: two different tests, a) and b); c) and d) ice front progress overlapped to the strips used for its detection in VR.

VR images was achieved through a trial-and-error process, overlapping different frames and identifying corresponding pixels and time steps.

Temperatures of the ice front propagation T_f were recalculated using the obtained results and perturbed by $\pm\ \Delta d$, $\pm\Delta x$ and $\pm\Delta t$, resulting in 27 graphs. Among these, the greatest source of uncertainty in Tf appeared to stem from Δd.

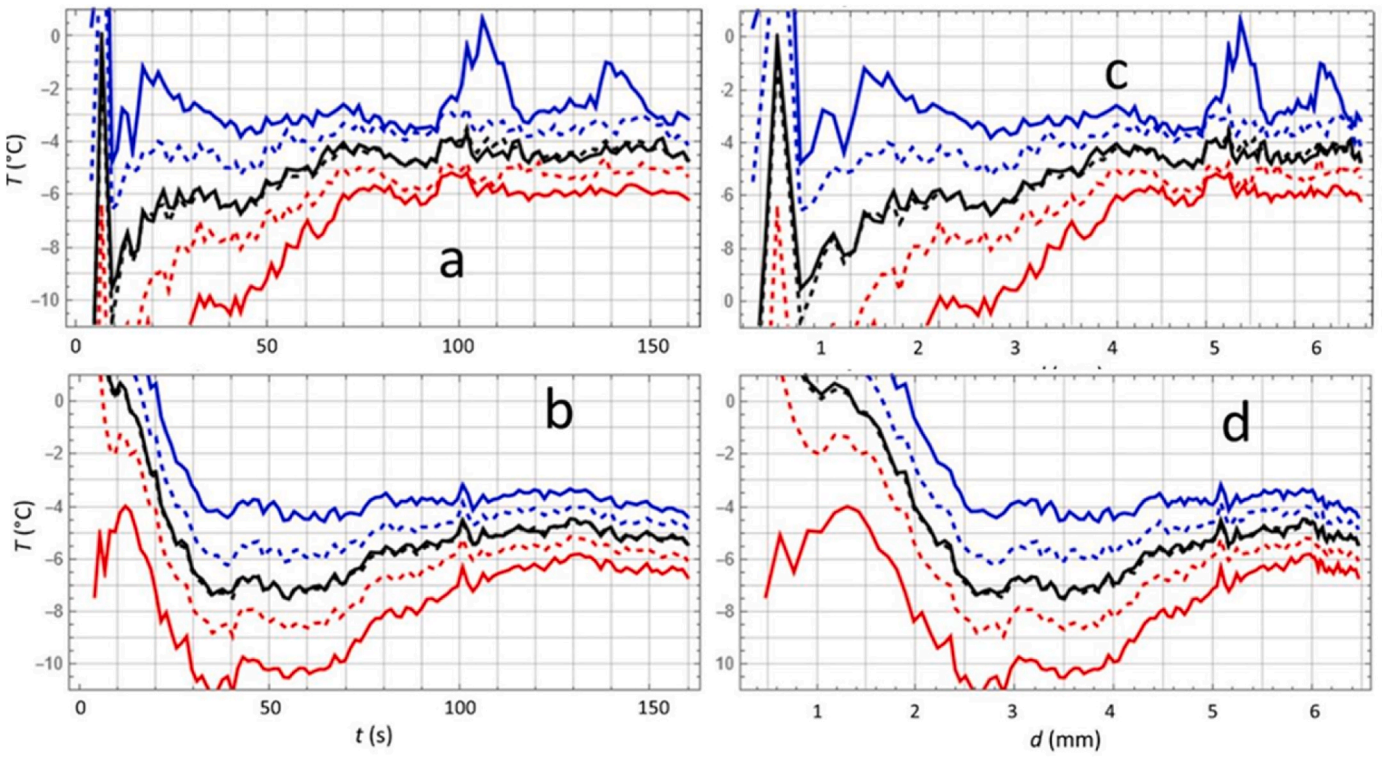

Fig. 8. Ice front temperature as a function of time t and the distance from the cold finger d, showing also the 0^{th} (full red), first (dotted red), second (dotted black), third (dotted blue) and fourth (full blue) quartiles; full black represents the average.

In addition to spatial and temporal resolutions, uncertainties related to temperature must also be considered. The IR camera's declared temperature resolution is finer than 0.1 °C, with an accuracy of ±1 °C, directly influencing the detection of T_f. The ice front propagation was also observed using the VR camera, identifying the transition between frozen and unfrozen meat portions by color changes (Fig. 3). This transition is detected with a resolution of 0.1 mm in VR, thereby corroborating the net transition detected by IR from frozen to unfrozen states. When this transition occurs between 60 s and 180 s, it is easily discernible due to the low temperature gradient and consistent trend in T_f (see Figs. 5d–. 7c and 7d). Conversely, during earlier stages (0 s–60 s), high variability is present, leading to greater uncertainty in ice front detection and significantly influencing T_f values.

The evolution of the ice front temperature is depicted in Fig. 8, showing its variation over both time and distance from the CF, alongside corresponding quartiles.

Overall, the uncertainty resulting from time and spatial synchronization between the visible and IR cameras yields 27 combinations X × D × T, with X = $\{x - \Delta x, x, x + \Delta x\}$; D = $\{d - \Delta d, d, d + \Delta d\}$; $T = \{t - \Delta t, t, t + \Delta t\}$ for both the first and second samples. Analysis reveals that vertical collimation represents the primary source of uncertainty, while time-related uncertainty is negligible in comparison to others.

Fig. 9 illustrates temperature trends detected by three thermocouples: the first applied to the CF, the second positioned in the middle of the tissue flap, and the third on its surface. From Fig. 9, it is evident that the CF temperature increases upon contact with the piece of flesh, reaches a peak, and then gradually decreases as heat is extracted by the cold finger. However, this decrease occurs over a much longer period than the typical duration of cryotherapy (60–80 s), rendering it inconsequential for data analysis. Notably, the temperature in the middle of the meat flap decreases more rapidly compared to that on its surface, due to its closer proximity to the CF. Unfortunately, these data cannot reliably predict the progression of the ice front because the positions of the thermocouples are not fixed but vary over time due to the meat's lack of rigidity before freezing.

A comparison with the results of the simulation model [10] can only be partially conducted. The cryo-probe temperature in the experiments was lower (ranging between −81 °C and −88 °C) compared to the −50 °C used in the model for clinical practice, as shown in Fig. 5a. Consequently, freezing occurred much faster, typically within 3–5 s (Fig. 4d), compared to the 60–80 s in the model. Further comparisons between model predictions and experimental results under identical conditions will be pursued in future studies. This will involve adjusting the numerical simulations to match the experimental conditions and comparing outcomes with predictions (see Section 3 of the Introduction).

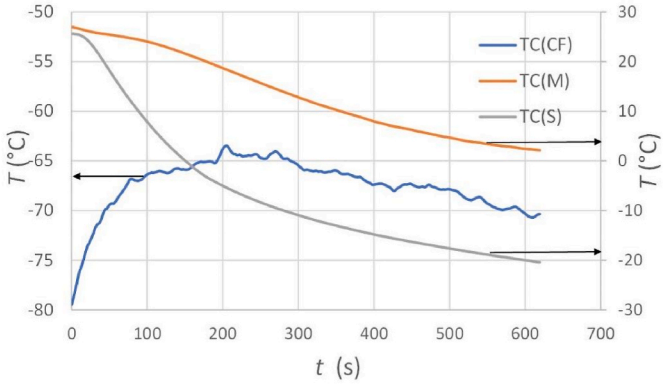

Fig. 9. Trends of the cold finger and meat flap temperatures as recorded by the applied thermocouples: TC(CF), thermocouple located on the cold finger; TC (M), thermocouple located in the center of the meat flap; TC(S), thermocouple located on the meat surface.

4. Comment on results

As previously noted by other researchers [13–15,18], replicating the dynamics of ice front propagation is challenging due to significant uncertainties and experimental difficulties. The following main sources of uncertainty have been identified.

1. Variability in the contact conditions between the CF and the flesh, potentially involving trapped air.
2. Manual correction of different viewpoints between the IR and VR cameras, leading to unavoidable uncertainties.
3. Lack of synchronization between the two camera systems.
4. Limited spatial resolution of the IR camera.
5. Uncertainty in temperature measurements by the IR camera.
6. Local heterogeneity in freezing patterns detected by the VR camera.

To enhance data quality, the following strategies are proposed.

1. Ensuring better contact between flesh and CF, possibly using a coupling liquid or conducting experiments in a vacuum or inert gas chamber.
2. Implementing a camera capable of simultaneous VR and IR detection.
3. Using a more suitable IR lens, such as one designed for microscopes, to improve magnification.
4. Calibration of IR cameras using proper-sized black bodies.

Processing the large volume of collected data requires significant time. Additionally, efforts must be made to minimize differences in initial temperatures among repeated tests to ensure better reproducibility of results.

5. Conclusions

This paper focuses on experiments conducted to monitor the progression of the ice front in heart tissues during cryotherapy. Freshly slaughtered pig hearts were sectioned and subjected to freezing using a cold finger, with visible and IR recordings used to track the advancement of the ice front.

The results effectively demonstrate how the ice front propagates within heart tissues, despite the experimental conditions differing somewhat from those used in clinical practice. Comparing these experimental findings with results from numerical simulations under similar conditions will provide insights into the expected outcomes during clinical applications. Therefore, this study presents an opportunity to analyze phase changes and their movement, aiming to better characterize the propagation of the ice front in biological tissues.

Future developement

As mentioned in the introduction, the numerical model developed in Ref. [10] will be executed under the varied experimental conditions detailed in this paper. This includes calibrating model parameters such as temperatures, heat fluxes, and distances. These calibrated parameters will facilitate simulating clinical practices, thereby enabling customization of therapy for patients of varying sizes, ages, races, etc.

Another aspect of the study will involve evaluating the thermophysical properties of the tissues involved, aiming to identify any differences among them and to refine the simulation accordingly.

CRediT authorship contribution statement

F. Barbero: Validation, Software, Investigation, Data curation. **G. Verona Rinati:** Validation, Supervision, Methodology. **G. Bovesecchi:** Writing – review & editing, Writing – original draft, Visualization, Validation, Supervision, Methodology, Investigation, Formal analysis,

Data curation. **S. Corasaniti:** Writing – review & editing, Writing – original draft, Visualization, Supervision, Methodology, Formal analysis. **M. Potenza:** Writing – review & editing, Writing – original draft, Methodology, Formal analysis, Data curation. **P. Coppa:** Writing – review & editing, Writing – original draft, Visualization, Validation, Supervision, Software, Methodology, Investigation, Formal analysis, Data curation, Conceptualization. **C. Pisano:** Writing – review & editing, Writing – original draft, Validation, Supervision, Investigation, Conceptualization.

Declaration of competing interest

The authors declare that they have no known competing financial interests or personal relationships that could have appeared to influence the work reported in this paper.

Data availability

Data will be made available on request.

Nomenclature

Acronyms

CF	Cold finger
CF PS	Cold finger power supply
CJ	Thermocouple cold junction
DAS	Digital Acquisition System
DHI	Digital Holographic Interferometry
FS	Flash strip
IR	Infra-Red
QTFF	Quick Time File Format
TC	Thermocouple
VR	Visible Range

Latin

d	radial distance from the cold finger
t	time
T	Temperature (K or °C)
x	transversal (tangential) distance

Greek

σ	standard deviation
Δ	difference (of temperature, time or position)

Subscript

f	ice front
0	initial(time)

References

[1] J.G. Andrade, P. Khairy, M. Dubuc, Catheter cryoablation, Circ Arrhythm Electrophysiol 6 (2013) 218–227, https://doi.org/10.1161/CIRCEP.112.973651.

[2] F. Barbero, G. Bovesecchi, P. Coppa, C. Passerone, V. Giaretto, Testing the physical core of cryoballoon probe: the medical needs behind a complex thermo-fluid dynamic behavior, in: AIPT, XVIII Convegno AIPT, Padova, 2017, pp. 125–134.

[3] J.S. Hermida, J. Chen, C. Meyer, S. Iacopino, G. Arena, N. Pavlovic, V. Velagic, S. Healey, D.L. Packer, H.-F. Pitschner, C. de Asmundis, M. Kuniss, G.B. Chierchia, Cryoballoon catheter ablation versus antiarrhythmic drugs as a first-line therapy for patients with paroxysmal atrial fibrillation: rationale and design of the international Cryo-FIRST study, Am. Heart J. 222 (2020) 64–72, https://doi.org/10.1016/j.ahj.2019.12.006.

[4] https://www.bostonscientific.com/en-US/products/catheters–ablation/polarx.html, (accessed on 21 March 2024), POLARx,(Accessed on 26 MArch 2024) (n.d.).

[5] J. Mojica, F. Lipartiti, M. Al Housari, G. Bala, S. Kazawa, V. Miraglia, C. Monaco, I. Overeinder, A. Strazdas, R. Ramak, G. Paparella, J. Sieira, L. Capulzini, A. Sorgente, E. Stroker, P. Brugada, C. De Asmundis, G.-B. Chierchia, Procedural safety and efficacy for pulmonary vein isolation with the novel Polarx^{TM} cryoablation system: a propensity score matched comparison with the arctic Front^{TM} cryoballoon in the setting of paroxysmal atrial fibrillation, J. Atr. Fibrillation 14 (2021), https://doi.org/10.4022/jafib.20200455.

[6] R. Narui, M. Tokuda, M. Matsushima, R. Isogai, K. Tokutake, K. Yokoyama, M. Hioki, K. Ito, S. Tanigawa, S. Yamashita, K. Inada, K. Shibayama, S. Matsuo, S. Miyanaga, K. Sugimoto, M. Yoshimura, T. Yamane, Incidence and factors associated with the occurrence of pulmonary vein narrowing after cryoballoon ablation, Circ Arrhythm Electrophysiol 10 (2017), https://doi.org/10.1161/CIRCEP.116.004588.

[7] T.J. Bunch, G.K. Bruce, S. Mahapatra, S.B. Johnson, D.V. Miller, A.V. Sarabanda, M.A. Milton, D.L. Packer, Mechanisms of phrenic nerve injury during radiofrequency ablation at the pulmonary vein orifice, J. Cardiovasc. Electrophysiol. 16 (2005) 1318–1325, https://doi.org/10.1111/j.1540-8167.2005.00216.x.

[8] K.M. Gürses, M.U. Yalçın, D. Koçyiğit, H. Yorgun, L. Şahiner, B. Kaya, N. Özer, K. Aytemir, M.A. Oto, OP-285 what lies beneath the cryoballoon ablation with the new arctic front advance cryoballoon: higher incidence of phrenic nerve palsy, Am. J. Cardiol. 113 (2014) S68, https://doi.org/10.1016/j.amjcard.2014.01.189.

[9] J. Martí-Almor, M.E. Jauregui-Abularach, B. Benito, E. Vallès, V. Bazan, A. Sánchez-Font, I. Vollmer, C. Altaba, M.A. Guijo, M. Hervas, J. Bruguera-Cortada, Pulmonary hemorrhage after cryoballoon ablation for pulmonary vein isolation in the treatment of atrial fibrillation, Chest 145 (2014) 156–157, https://doi.org/10.1378/chest.13-0761.

[10] M. Potenza, C. Pisano, P. Coppa, G. Bovesecchi, S. Corasaniti, F. Barbero, Numerical simulations of temperature inside the heart tissues to evaluate the performances of cryoablative probe, Int. Commun. Heat Mass Tran. 146 (2023) 106877, https://doi.org/10.1016/j.icheatmasstransfer.2023.106877.

[11] H.H. Pennes, Analysis of tissue and arterial blood temperatures in the resting human forearm, J. Appl. Physiol. 1 (1948) 93–122, https://doi.org/10.1152/jappl.1948.1.2.93.

[12] Y. Zhang, K. Du, J.P. He, L. Yang, Y.J. Li, Impact factors analysis of the enthalpy method and the effective heat capacity method on the transient nonlinear heat transfer in phase change materials (PCMs), Numeri Heat Transf A Appl 65 (2014) 66–83, https://doi.org/10.1080/10407782.2013.811153.

[13] Z.-S. Deng, J. Liu, Numerical simulation of 3-D freezing and heating problems for combined cryosurgery and hyperthermia therapy, Numeri Heat Transf A Appl 46 (2004) 587–611, https://doi.org/10.1080/10407780490487740.

[14] Y. Rabin, A. Shitzer, Combined solution of the inverse stefan problem for successive freezing/thawing in nonideal biological tissues, J. Biomech. Eng. 119 (1997) 146–152, https://doi.org/10.1115/1.2796073.

[15] Y. Rabin, A. Shitzer, Numerical solution of the multidimensional freezing problem during cryosurgery, J. Biomech. Eng. 120 (1998) 32–37, https://doi.org/10.1115/1.2834304.

[16] P.L. Altman, D.S. Dittmer, Respiration and Circulation, Federation of American Societies for Experimental Biology, Bethesda MD, 1971.

[17] F.C. Wessling, P.L. Blackshear, The thermal properties of human blood during the freezing process, J. Heat Tran. 95 (1973) 246–249, https://doi.org/10.1115/1.3450035.

[18] G. Zhao, D. Luo, D. Gao, Universal model for intracellular ice formation and its growth, AIChE J. 52 (2006) 2596–2606, https://doi.org/10.1002/aic.10851.

[19] P.P. Lelovas, N.G. Kostomitsopoulos, T.T. Xanthos, A comparative anatomic and physiologic overview of the porcine heart, J Am Assoc Lab Anim Sci 53 (2014) 432–438.

[20] D.D. Soerensen, S. Clausen, J.B. Mercer, L.J. Pedersen, Determining the emissivity of pig skin for accurate infrared thermography, Comput. Electron. Agric. 109 (2014) 52–58, https://doi.org/10.1016/j.compag.2014.09.003.

[21] A. Gunjal, G. Kumar Sinha, S. Narayan, A. Srivastava, M.D. Atrey, Simultaneous tracking of freezing front and associated temperature-distribution using lensless Fourier transform digital holographic interferometry with potential application in cryosurgery, Exp. Therm. Fluid Sci. 139 (2022) 110730, https://doi.org/10.1016/j.expthermflusci.2022.110730.

[22] https://www.flir.it/browse/rampd-and-science/high-performance-cameras/fixed-entry-level-cameras/. (Accessed 21 March 2024). FLIR A6751, (Accessed on 26 March 2024) (n.d.

[23] https://www.flir.it/products/flir-research-studio?vertical=rd+science&segment=solutions. (Accessed 21 March 2024). FLIR Research, (Accessed on 26 March 2024) (n.d.).

[24] https://www.scilab.org/. (Accessed 21 March 2024). Scilab, (Accessed on 26 March 2024) (n.d.).

[25] https://www.wolfram.com/mathematica/. (Accessed 21 March 2024). Mathematica, (Accessed on 26 March 2024) (n.d.